# Influence of high mean stresses on lifetime and damage of the martensitic steel X10CrNiMoV12-2-2 in the VHCF-regime

**Tilmann Beck[1,*], Stephan Kovacs[1], Lorenz Singheiser[1]**

[1] Institute of Energy and Climate Research (IEK-2), Forschungszentrum Jülich, Jülich 52425, Germany
* Corresponding author: t.beck@fz-juelich.de

Martensitic 9-12% Cr-steels are widely applied in steam turbines. In the low pressure rotor blades, fatigue loadings at several 100 Hz induced by the inhomogeneous flow field behind the vanes are superimposed by high mean stress due to centrifugal forces. Using an ultrasonic fatigue testing machine and in-depth microstructure analyses, the present study investigates the influence of mean stresses at load ratios up to $R$ = 0.7 on the VHCF behavior with an ultimate cycle number of $2 \cdot 10^9$.
From $R$ = -1 (no mean stress) up to $R$ = 0.7 crack initiation changes consistently from the surface to internal inclusions at a cycle number around $4 \cdot 10^7$. Fractography indicates that fine grained areas around the inclusions only occur for R=-1. With increasing load ratio, fractures are observed at increasing cycle numbers. In spite of this fact and in spite of considerable cyclic creep at load ratios up from $R$ = 0.5, the fracture mechanics approach proposed by Murakami consistently describes the lifetime behavior for load ratios up to $R$ = 0.5 over 4 decades of lifetime. The contribution will give a comprehensive overview of these findings together with detailed microstructure studies of the fracture surfaces.

VHCF, Cr steel, turbine blade steel, mean stress, fatigue damage

## 1. Introduction

The research activities in the field of fatigue with very high cycle numbers (VHCF) were massively expanded in the past decade. Overviews of the basic mechanisms of VHCF are given in [1-4]. Generally, materials can be distinguished into two types according to their VHCF behavior. Type I materials are single-phase, inclusion-free materials like pure aluminum or copper. At very low stress amplitudes and high number of cycles, fatigue cracks in this type of materials usually originate at persistent slip bands (PSB), even at stress amplitudes below the PSB threshold, induced by local stress concentration at surface roughnesses. Type II materials on the other hand are multi-phase materials with a characteristic transition in the fracture mechanism between $10^7$ and $10^8$ cycles which commonly results in a multi-stage $S$-$N$ curve as shown by Mughrabi in [5]. At high stress amplitudes, i.e. at low number of cycles to failure, fractures mainly occur at surface inclusions or at PSBs. At lower stress amplitudes in the VHCF-regime, subsurface cracks in the form of so-called "fish-eye fractures" occur, primarily originating from inclusions. Typically, subsurface fractures are reported in connection with the formation of a small zone around the inclusion called optical dark area (ODA), fine granular facets (FGA) or granular bright facets (GBF).
Such a multistage fatigue life behavior for type II metals has been found for rotating bending fatigue of Cr-Mo and high carbon bearing steels [4, 6] and also for a 42CrMo4 tempered steel and some aluminum alloys at axial fatigue loading [3, 4, 7, 8]. The stages are mainly influenced by inclusion size, surface roughness and notch factor. The critical inclusion size for internal fracture is not fixed and depends on many factors e.g. yield stress, and typically ranges from 5 μm to 500 μm. For high-strength steels, the critical inclusion size is in the range of 10 μm [2]. In this context, Murakami proposed a fracture mechanics approach, the $\sqrt{area}$-concept, to correlate the inclusion sizes with VHCF life [9]. He treated inclusions as preexisting short cracks and, based on this assumption, calculated fatigue strength, fatigue life and stress intensity factor of the crack taking into account the largest inclusion of the specimen.
However, especially the influence of superimposed mean stresses on the VHCF behavior of metallic materials is not yet sufficiently investigated. Shiozawa *et al.* [10] and Sakai *et al.* [11] investigated

the mean stress influence up to a load ratio of 0.5 on the HCF and VHCF behavior of a high-strength bearing steel (tensile strength: 2316 MPa, HV749) with high compressive residual surface stresses (-373 MPa). The VHCF tests were conducted up to an ultimate numbers of cycles of $2 \cdot 10^8$ and $10^9$, respectively. Fatigue fracture is generally initiated at inclusions with an average size of 17 µm. With increasing *R* the slope of the *S-N* curves becomes extremely flat. For $R = 0$ and 0.5 the measured fatigue limits lie distinctly below the Goodman approximation.
To extend the relatively good knowledge of VHCF behavior of high strength fully martensitic steels to ferritic steels with intermediate strength and relatively high ductility typically used for steam turbine blades, the present study deals with the VHCF behavior of a typical representative of this type of materials up to $2 \cdot 10^9$ cycles. The investigated material is a martensitic 12% Cr steel frequently used for turbine blades in power plant applications. For this class of steels, the influence of mean stresses on the fatigue behavior is a main issue. Especially the last stages of low pressure steam turbine blades have to sustain fatigue loads with extremely high superimposed mean stresses due to a rotational speed of 50 Hz in combination with blade lengths of up to 1.5 m. High-frequency loading occurs due to inhomogeneous flow fields behind the vanes. With load frequencies above 2000 Hz and a component life up to 30 years, the number of cycles clearly reaches the very high cycle fatigue (VHCF) region above $10^9$ cycles. Hence, VHCF loading must be considered in the design of low-pressure turbine blades. Currently, such turbine blades are designed with high safety coefficients based on S-N curves assumed to approach an asymptotic fatigue limit at $N > 10^7$ load cycles. Nevertheless, blade failures at high number of cycles still occur at corrosion pits or even at blade roots without environmental influence [12-16].

## 2. Materials and methods

The material tested in this study is a martensitic 12% Cr steel used for low pressure steam turbine blades in power generation. The chemical composition is shown in Table 1.

Table 1
Chemical composition of X10CrNiMoV12-2-2

| element | C | Cr | Ni | Mo | Mn | V | Si |
|---|---|---|---|---|---|---|---|
| weight-% | 0.117 | 11.4 | 2.70 | 1.64 | 0.70 | 0.31 | 0.23 |

To obtain a martensitic microstructure, the blades were hardened by annealing at 1040 °C for 60 min and subsequent compressed air cooling. For stress relief purposes, the blades were subsequently tempered at 660 °C for 3 h followed by annealing at 640 °C for 4 h and very slow furnace cooling. The resulting highly tempered martensitic microstructure has finely distributed Cr-carbides with diameters of around 100 nm along the martensite laths and the former austenite grain boundaries. Precipitation-hardening results in high ultimate tensile strength combined with a sufficient elongation at fracture (Table 2). Due to its heat treatment, the microstructure is stable up to temperatures as high as 600°C and ensures safe application of this steel for power plant applications.

Table 2
Mechanical properties of X10CrNiMoV12-2-2 at room temperature

| | |
|---|---|
| Vickers hardness | 334 HV |
| Yield strength | 843 MPa |
| Ultimate tensile strength | 1001 MPa |
| Elongation at fracture | 17.7 % |
| Contraction at fracture | 58 % |
| Young´s Modulus | 213 GPa |

Subsequently, cylindrical rods were eroded from the blade root by electro-discharge-machining and turned to the final specimen geometry with cylindrical gauge length and a diameter of 3 mm. Fig. 1shows the geometry for tests without mean stress ($R$ = -1), Fig. 2 the specimen shape for tests with superimposed mean stresses ($R$ > 0).

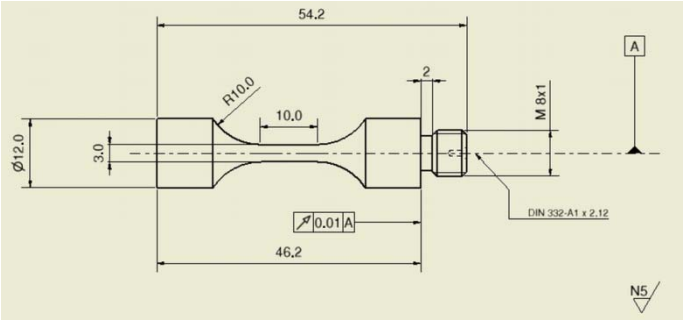


Figure 1. Specimen geometry for $R$ = -1 fatigue tests.

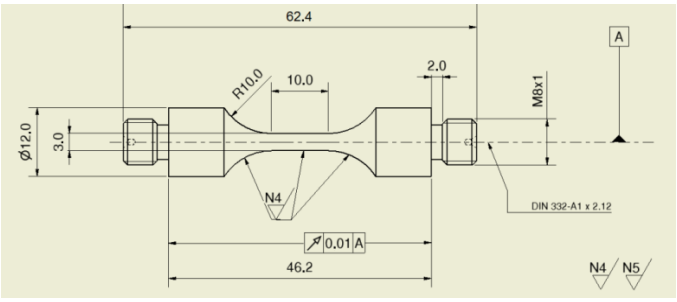


Figure 2. Specimen geometry for $R$ > 0 fatigue tests.

Finally, the samples were ground with SiC abrasive paper and subsequently mechanically polished. The residual stresses in the polished state were determined to -34 ± 16 MPa by X-ray diffraction using the sin2$\psi$-method.

Testing system is the Ultrasonic Fatigue Testing Equipment (UFTE) developed and manufactured by Boku Wien attached to an Instron 5967 load frame for fatigue tests with superimposed mean stresses. The experimental setup is similar to that described in [17]. For tests at $R$ = -1, the specimens are clamped at one end to allow free oscillation. The UFTE system develops a standing wave during oscillation. Ultrasonic fatigue tests were performed in displacement control at constant-amplitude tension-compression loading in laboratory air at room temperature. Assuming linear-elastic behavior in the VHCF regime, strain gauges can be utilized to calibrate the system prior to the experiments by using the linear correlation between displacement and stress in the gauge section [18]. To limit self-heating of the specimen during loading, a load pulse / pause ratio of 80-200 ms / 800-1200 ms was applied together with forced air cooling of the specimen. To analyze the influence of high mean stresses, load ratios ranging from -1 up to 0.7 were applied. Additionally, load controlled fatigue tests were conducted using an Instron 1603 electromagnetic resonance testing machine at frequencies of about 100 Hz to investigate the frequency influence on fatigue life. An ultimate number of cycles of $2 \cdot 10^9$ was chosen for the tests conducted with the ultrasonic device and of $10^8$ for the electromagnetic fatigue testing machine, respectively.

After fatigue testing, fracture surfaces of failed specimens were observed by SEM, paying particular attention to classification of the fracture modes of surface and subsurface fracture at persistent slip bands and inclusions, respectively, and analyzing diameters as well as chemical composition of the inclusions.

# 3. Results and discussion

## 3.1 Fatigue life analysis and load ratio influence

The fatigue data of X10CrNiMo12-2-2 previously presented in [19] are shown in Fig. 3 with load ratios ranging between $R$ = -1 and $R$ = 0.7. In the *S-N* curves, no "two step" behavior indicating separate fatigue limits for surface and sub-surface cracks could be observed. Furthermore, for $R$ = -1, there is a smooth transition in the curve from the literature data by Zhou et al. [20] for the LCF (grey symbols) to the HCF (blue symbols) data at approximately $10^5$ load cycles. Considering all data plotted for $R$ = -1, no significant frequency effect can be seen in a frequency range of over four orders of magnitude ranging from 1 Hz up to 20 kHz. Literature data of the investigated steel for load ratios higher than -1 is not available. Hence, the ultrasonic fatigue tests are considered to be representative for a wide frequency range allowing to reach high cycle numbers within appropriate time.

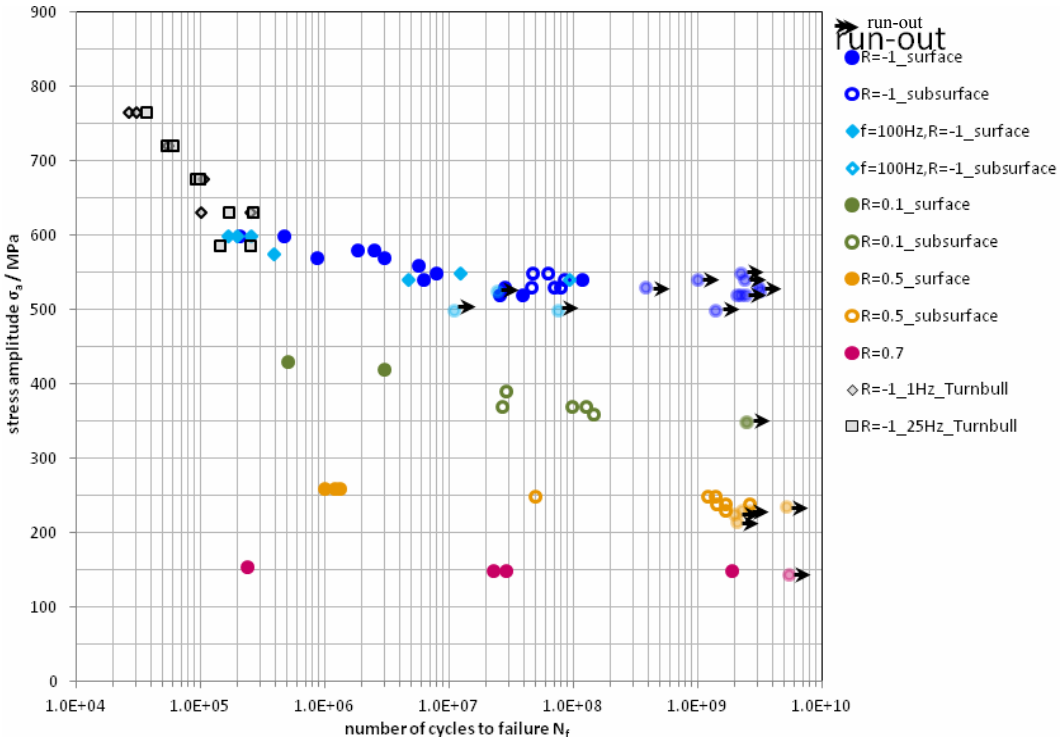


Figure 3. Stress amplitude vs. number of cycles to failure for load ratios $R$ = -1. 0.1, 0.5 and 0.7 at RT.

In Fig. 3, filled symbols mark fractures originating from the surface (persistent slip bands or surface inclusions) and open symbols indicate volume fractures of subsurface inclusions. A quite narrow transition band from surface to internal fractures between approximately $2 \cdot 10^7$ and $4 \cdot 10^7$ load cycles exists independent of the load ratio. As expected, a quite large scatter in fatigue life was observed. Fatigue strength and the slope of the curves decrease with increasing load ratio. The huge scatter of the curves is mainly caused by the inclusion size distribution.
Another conspicuous feature of the *S-N* curves is the correlation between the load ratio and the highest numbers of cycles to failure: While for $R$ = -1 failure only appears at less than $10^8$ cycles (with one exception), there are fractures above $10^8$ cycles for $R$ = 0.1. For $R$ = 0.5 and $R$ = 0.7, failure even occurred above $10^9$ cycles close to the defined run-out limit. Despite the small amount of data for higher load ratios, this trend is obvious and, at least for this material, has not been observed before and is subject of further research.

Furthermore, different approaches were applied to evaluate the fatigue strengths at the investigated load ratios: Because at load ratios $R > 0$ the database is insufficient for statistical evaluation of fatigue strength, a pragmatic approach is used. As the flat slope of the *S-N* curves (Fig. 3) is a convenient precondition for assessing the fatigue limit, the fatigue strength is defined as the highest stress amplitude where specimens still not failed. Hence, the following fatigue strengths were determined: 350 MPa for $R = 0.1$, 230 MPa for $R = 0.5$ and 145 MPa for $R = 0.7$. For $R = -1$, the arcsin$\sqrt{P}$-method [21] was applied for calculating the fatigue strength, taking all data points in the vicinity of the run-out specimens into account. The resulting fatigue limit for $R = -1$ is a stress amplitude $\sigma_a$ of 495 MPa.

### 3.2 Fractographiy-based evaluation of fatigue life

In the next step, crack initiating defects were identified and analyzed using SEM and EDX. Up to about $10^7$ cycles, most fractures initiated at persistent slip bands (PSBs) or at surface inclusions. Both HCF fracture types were observed for fatigue lives up to $4 \cdot 10^7$ cycles at all investigated load ratios. A more detailed investigation of the fracture surfaces is given in [19].

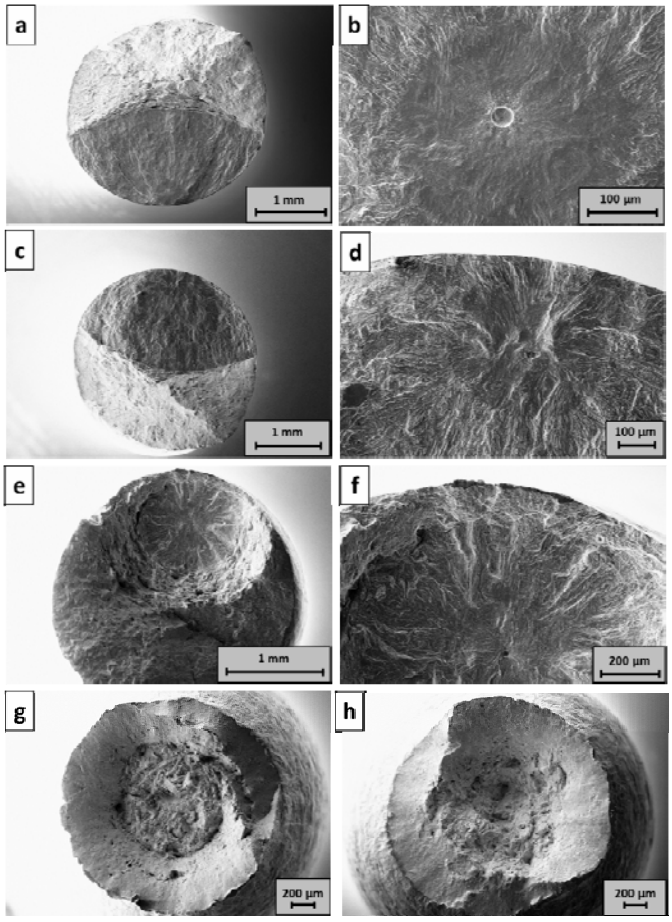


Figure 4. Fracture surfaces of typical fish-eye cracks: (a, b) $\sigma_a = 550$ MPa, $R = -1$, $N_f = 4.66 \cdot 10^7$; (c, d) $\sigma_a = 370$ MPa, $R = 0.1$, $N_f = 1.24 \cdot 10^8$; (e, f) $\sigma_a = 250$ MPa, $R = 0.5$, $N_f = 1.21 \cdot 10^9$; (g) $\sigma_a = 155$ MPa, $R = 0.7$, $N_f = 2.35 \cdot 10^5$; (h) $\sigma_a = 150$ MPa, $R = 0.7$, $N_f = 2.28 \cdot 10^7$.

In the VHCF-regime, i.e. at fatigue lives above approximately $4 \cdot 10^7$ cycles, fish-eye cracks, which are characteristic for VHCF failure of high strength steels [5], are found in all fracture surfaces (Fig. 4). The frequently observed "optical dark areas" (ODAs) [22-25] are difficult to identify in this steel.

In Fig. 4b) for $R$ = -1, an ODA is visible in the region directly above the inclusion. Such structures could be observed in several specimens for $R$ = -1, but were never found in samples fatigued at higher load ratios. Examples are given in Fig. 4d) and f).
Some uncertainty remains in this observation because ODAs are generally very difficult to detect in this steel. In [19], microstructural investigations were performed via focused ion beam technique (FIB) and SEM of cross-sections perpendicular to the fatigue crack surface close to the crack initiating inclusion. The results showed the presence of a nanocrystalline area around the inclusion only for $R$ = -1. Based on this observation, a possible reason for the $R$-dependency of the highest observed number of cycles to failure is given in [19].

Furthermore, there is a change of the fracture surface profile with increasing load ratio. At higher load ratios, the fish-eyes become more distinguished and a step-like transition develops between the fish-eye and the residual fracture which indicates the occurrence of cyclic creep and plastic deformation. As shown by displacement measurements of the specimens during the fatigue tests in [19], increasing load ratio leads to higher total mean strains, i.e. plateau values of 0.4% and 4.5% for $R$ = 0.1 and $R$ = 0.5, respectively. At $R$ = 0.7, steady cyclic creep occurs during the entire test. Additional fatigue tests at high stress amplitudes were performed showing weak cyclic softening of this steel in accordance with [26] for a similar kind of 12% Cr steel. The dominance of cyclic creep on deformation and failure at $R$ = 0.7 corresponds to the fracture surface depicted in Fig. 4g) and h) showing a “tensile test like” cup-cone fracture without any distinct fatigue features. However, it should be noted that even at this high load ratio fatigue lives clearly above $10^7$ have been reached.

For the fish-eye fractures at other load ratios, inclusion sizes and compositions as well as the area of the fish-eyes were determined by SEM and EDX. For all fractures, the crack initiated at oxide inclusions in the middle of the fish-eye with compositions either $CaO{\cdot}Al_2O_3$ or $MgO{\cdot}Al_2O_3$. However, the crucial factor for fatigue life is the diameter of crack inducing inclusions, following a normal distribution and ranging from 16 µm up to 45 µm in this test series. To consider the inclusion size dependency on fatigue life, the $\sqrt{area}$-concept of Murakami [9] was applied. The $\sqrt{area}$-parameter represents the inclusion size perpendicular to the applied maximum stress, which is treated equivalent to a fatigue crack of equal size. By means of fracture mechanics, this leads to Eq. (1) for the fatigue strength:

(1)

$HV$ is the hardness of the material and $\alpha$ a material constant describing the influence of load ratio. $C$ is 1.56 for internal defects and 1.43 for subsurface cracks, respectively. At first, the material constant $\alpha$ for the $R$-dependency of the fatigue limit needs to be determined from the slope of the fatigue strength vs. (1-$R$)/2 curve. In the present case, $\alpha$ is 0.546. In the next step, $\sigma_a/\sigma_W$ can be plotted against the number of cycles to failure in a linear graph (Fig. 5). In this plot, the huge scatter of the $S$-$N$ curves could be reduced to less than one order of magnitude, so the fatigue data of load ratios from -1 up to 0.5 can be described in a single curve in a fatigue life range of more than four orders of magnitude. The Murakami approach is convenient for describing the curve both in the HCF and the VHCF-regime and independent of load ratio. Thus, the $\alpha$-parameter of 0.546 seems to be accurate for describing the dependency of fatigue strength on load ratio of the present material. An evaluation of the $R$ = 0.7 data and a deeper analysis of the obtained $\alpha$ value is given in [19].

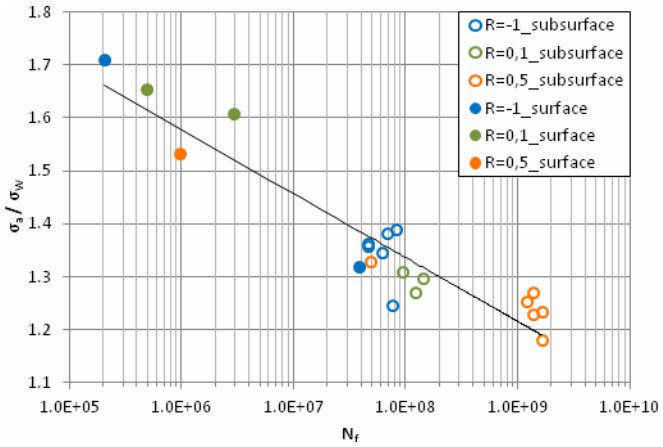


Figure 5. Modified *S-N* curve according to the *√area*-concept proposed by Murakami.

### 3.3 Crack growth threshold evaluation

Another appropriate data evaluation method is shown in [27, 28]. In the present work, this approach proposed by Döker is applied to small fatigue cracks assuming the fracture inducing inclusion sizes being identical with the initial crack length. Based on the linear elastic fracture mechanics, the threshold stress intensity factor $\Delta K_{th}$ can be plotted vs. the load ratio $R$. As mentioned in [27], only positive $R$ can be used and given the fact that no fracture inducing inclusions were visible for fractured specimen at $R = 0.7$ (see Fig. 4g) and h)), this approach is only applied for fatigue data of $R = 0.1$ and 0.5. Initially, $\Delta K_{th}$ needs to be calculated. Assuming a circle shaped volume crack with the diameter of the crack initiating inclusion, Eq. (1) and Eq. (2) can be used as good approximations, where $a_{incl}$ is the mean size of all measured inclusions and $\Delta\sigma_D$ and $\sigma_{D,max}$ are the corresponding fatigue strength values.

(2)

$$K_{max} = \frac{2}{\pi}\sigma_{D,max}\sqrt{\pi a_{incl}} \qquad (3)$$

According to [27], a $\Delta K_{th}$–$R$ curve can be derived from the above values (continuous line in Fig. 6). The curve is separated into multiple sections described by different equations (see Fig. 6). Here, the two curves nearly overlap at negative $R$. For $R < 0$, the green dotted line is valid and the threshold value asymptotically approaches $\Delta K_0$. The red dotted line represents a downward oriented parabola which intersects with the positive $R$-axis at $R = -1$ and with the $\Delta K_{th}$ –axis at $\Delta K_{th} = K_{max,0}$. The different shape of the curves compared with [27] probably is due to the distinctly smaller crack length considered in the present study. Additionally, Fig. 6 shows the $\Delta K$ values calculated from the obtained fatigue test data using the stress amplitudes and the crack inducing inclusion sizes (blue diamonds). Note that for this evaluation only fractures close to the observed run-outs (see Fig. 3) were taken into account. Referring to the work of Grad et al. [29], $\Delta K$ was also calculated using the sizes of the ODAs found at $R = -1$ (green triangles).

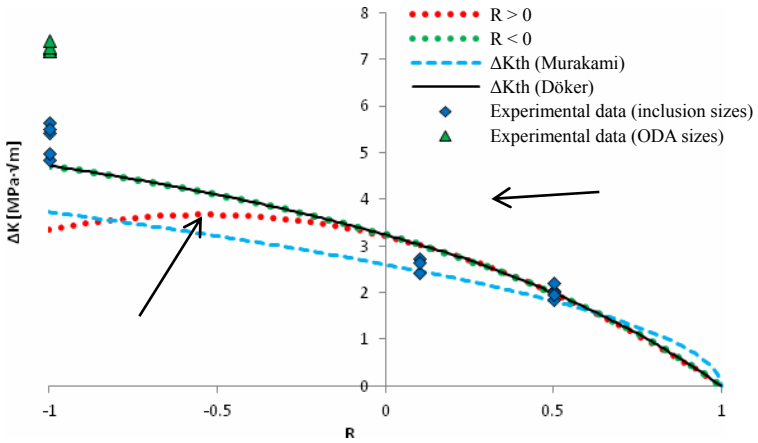


Figure 6. Threshold curves according to Döker and Murakami.

As expected, the data points for $R$ = 0.1 and 0.5 lie close to the approximation curve. For $R$ = -1, the data points calculated from the inclusion sizes are slightly above the calculated threshold value. The values considering the ODA sizes are around 7.3 MPa√m and with this lie well above the approximation curve. This difference indicates that, for $R$ = -1, crack closure effects, which are not considered in the applied fracture mechanics approach, are an important issue.
Concerning the relatively high ductility of the investigated 12% Cr steel, crack closure effects due to residual stresses near the crack tip are probably much more pronounced than in the high-strength 100Cr6 examined in [29]. The same conclusions can be drawn from the comparison of the individually calculated $\Delta K$ values with the $\Delta K_{th}$-$R$ curve proposed by Murakami (blue dashed line in Fig. 6), which is determined according to Eq. (4) with the material hardness HV, the $\sqrt{area}$ parameter and the material constant $\alpha$.

(4)

## 4. Summary

1. No frequency effect was found for fatigue tests with zero mean stress in a frequency range above four orders of magnitude.
2. In the LCF/HCF-regime, specimens either failed by cracks initiated at PSBs or surface inclusions. Above $2 \cdot 10^7$ - $4 \cdot 10^7$ load cycles, fish-eye cracks were found originating from oxide inclusions. The inclusion diameters ranged from 16 µm up to 45 µm and follow a normal extreme value distribution. The inclusion size has a decisive influence on fatigue life as shown by the modified $S$-$N$ curve proposed by Murakami [9]. The $\alpha$-parameter describing the load ratio dependency was determined to 0.546 and was in the vicinity of $\alpha$ values measured in recent investigations at other high-strength steels. Thus, the $\sqrt{area}$-concept is well applicable for this steel in a large range of load ratios ($-1 < R < 0.5$).
3. For $R$ = 0.7, the fatigue fracture surfaces are similar to quasi-static tensile fractures with high deformation and sample elongation due to extremely pronounced cyclic creep.

4. ODAs were only found for fatigue tests at $R = -1$. A reason for this may be reduced crack closure at $R > 0$, which has to be proven by further investigations of fracture surfaces by means of an SEM after FIB preparation of sections perpendicular to the crack surface.
5. The evaluation of the threshold values according to Döker was applied to short cracks. The results also indicate that crack closure effects may play an important role in connection with the ODA formation.

## Acknowledgements

The authors gratefully acknowledge funding of this study by the Deutsche Forschungsgemeinschaft (DFG).

## References

[1] C. Berger, B. Pyttel, D. Schwerdt, Beyond HCF - Is there a fatigue limit?, Materialwissenschaften und Werkstofftechnik, 39 (2008) 769-776.
[2] S.X. Li, Effects of inclusions on very high cycle fatigue properties of high strength steels, Int. Mater. Rev., 57 (2012) 92-114.
[3] H. Mughrabi, Fatigue, an everlasting materials problem - still en vogue, Procedia Engineering, 2 (2010) 3-26.
[4] T. Sakai, Review and Prospects for Current Studies on Very High Cycle Fatigue of Metallic Materials for Machine Structural Use, International Journal of Fatigue, 3 (2009) 425-439.
[5] H. Mughrabi, Specific features and mechanisms of fatigue in the ultrahigh-cycle regime, International Journal of Fatigue, 28 (2006) 1501-1508.
[6] T. Sakai, M. Takeda, K. Shiozawa, Y. Ochi, M. Nakajima, T. Nakamura, N. Oguma, Experimental evidence of duplex S-N characteristic's in wide life region for high strength steels, China Higher Education Press Beijing, Beijing, 1999.
[7] H.W. Höppel, L. May, M. Prell, M. Göken, Influence of grain size and precipitation state on the fatigue lives and deformation mechanisms of CP aluminium and AA6082 in the VHCF-regime, International Journal of Fatigue, 33 (2011) 10-18.
[8] Q.Y. Wang, C. Bathias, N. Kawagoishi, Q. Chen, Effect of inclusion on subsurface crack initiation and gigacycle fatigue strength, International Journal of Fatigue, 24 (2002) 1269-1274.
[9] Y. Murakami, S. Kodama, S. Konuma, Quantitative evaluation of effects of non-metallic inclusions on fatigue strength of high strength steels. I: Basic fatigue mechanism and evaluation of correlation between the fatigue fracture stress and the size and location of non-metallic inclusions, International Journal of Fatigue, 11 (1989) 291-298.
[10] K. Shiozawa, T. Hasegawa, Y. Kashiwagi, L. Lu, Very high cycle fatigue properties of bearing steel under axial loading condition, International Journal of Fatigue, 31 (2009) 880-888.
[11] T. Sakai, Y. Sato, Y. Nagano, M. Takeda, N. Oguma, Effect of stress ratio on long life fatigue behavior of high carbon chromium bearing steel under axial loading, International Journal of Fatigue, 28 (2006) 1547-1554.
[12] Z. Mazur, A. Hernández-Rossette, R. García-Illescas, Investigation of the failure of the L-0 blades, Engineering Failure Analysis, 13 (2006) 1338-1350.
[13] W.-Z. Wang, F.-Z. Xuan, K.-L. Zhu, S.-T. Tu, Failure analysis of the final stage blade in steam turbine, Engineering Failure Analysis, 14 (2007) 632-641.
[14] Z. Mazur, R. Garcia-Illescas, J. Porcayo-Calderon, Last stage blades failure analysis of a 28 MW geothermal turbine, Engineering Failure Analysis, 16 (2009) 1020-1032.
[15] Z. Mazur, R. Garcia-Illescas, J. Aguirre-Romano, N. Perez-Rodriguez, Steam turbine blade failure analysis, Engineering Failure Analysis, 15 (2008) 129-141.

[16] R. Ebara, Long-term corrosion fatigue behaviour of structural materials, Fatigue Fract. Eng. Mater. Struct., 25 (2002) 855-859.
[17] C. Bathias, K. El Alami, T.Y. Wu, Influence of mean stress on ti6a14v fatigue crack growth at very high frequency, Engineering Fracture Mechanics, 56 (1997) 255-264.
[18] S. Stanzl-Tschegg, Ultrasonic Fatigue, in: K.H.J.B. Editors-in-Chief: , W.C. Robert, C.F. Merton, I. Bernard, J.K. Edward, M. Subhash, V. Patrick (Eds.) Encyclopedia of Materials: Science and Technology (Second Edition), Elsevier, Oxford, 2001, pp. 9444-9449.
[19] S. Kovacs, T. Beck, L. Singheiser, Influence of mean stresses on fatigue life and damage of a turbine blade steel in the VHCF-regime, International Journal of Fatigue (accepted for publication), (2012).
[20] Zhou, Turnbull, Influence of pitting on the fatigue life of a turbine blade steel, Fatigue Fract. Eng. Mater. Struct., 22 (1999) 1083-1093.
[21] D. Dengel, Die arc sin √P-Transformation — ein einfaches Verfahren zur grafischen und rechnerischen Auswertung geplanter Wöhlerversuche, Materialwissenschaft und Werkstofftechnik, 6 (1975) 253-261.
[22] Y. Murakami, T. Nomoto, T. Ueda, On the mechanism of fatigue failure in the superlong life regime (N>107 cycles). Part 1: influence of hydrogen trapped by inclusions, Fatigue Fract. Eng. Mater. Struct., 23 (2000) 893-902.
[23] Y. Murakami, T. Nomoto, T. Ueda, On the mechanism of fatigue failure in the superlong life regime (N>107 cycles). Part II: influence of hydrogen trapped by inclusions, Fatigue Fract. Eng. Mater. Struct., 23 (2000) 903-910.
[24] T. Nakamura, H. Oguma, Y. Shinohara, The effect of vacuum-like environment inside sub-surface fatigue crack on the formation of ODA fracture surface in high strength steel, Procedia Engineering, 2 (2010) 2121-2129.
[25] Z.G. Yang, S.X. Li, Y.D. Li, Y.B. Liu, W.J. Hui, Y.Q. Weng, Relationship among fatigue life, inclusion size and hydrogen concentration for high-strength steel in the VHCF regime, Materials Science and Engineering: A, 527 (2010) 559-564.
[26] T. Petersmeier, U. Martint, D. Eifler, H. Oettelt, Cyclic fatigue loading and characterization of dislocation evolution in the ferritic steel X22CrMoV121, International Journal of Fatigue, 20 (1998) 251-255.
[27] H. Döker, Fatigue crack growth threshold: implications, determination and data evaluation, International Journal of Fatigue, 19 (1997) 145-149.
[28] H. Döker, Schwellenwert für Ermüdungsrissausbreitung: Bestimmung und Anwendung, Fortschritte der Bruch- und Schädigungsmechanik, (2002) 9-18.
[29] P. Grad, B. Reuscher, A. Brodyanski, M. Kopnarski, E. Kerscher, Mechanism of fatigue crack initiation and propagation in the very high cycle fatigue regime of high-strength steels, Scripta Materialia, 67 (2012) 838-841.